Angular distribution of near-threshold photoelectrons from resonance-enhanced multiphoton ionization of argon

Chuanpeng Cao,[1] Min Li,[1,*] Jintai Liang,[1] Jiaqing Yan,[1] Keyu Guo,[1] Zichen Li,[1] Yang Liu,[1] Yueming Zhou,[1] and Peixiang Lu[1,2]

[1]*School of Physics and Wuhan National Laboratory for Optoelectronics, Huazhong University of Science and Technology, Wuhan 430074, China*

[2]*Optics Valley Laboratory, Wuhan 430074, China*

(Received 5 July 2022; accepted 6 September 2022; published 20 September 2022)

We experimentally study the angular distribution of near-threshold photoelectrons of argon in the multiphoton-ionization regime. Those near-threshold photoelectrons are released from atoms by a weak 800-nm laser field and a strong 400-nm laser field with parallel polarizations. In the laser polarization direction, the yield of the near-threshold photoelectron oscillates with twice the 800-nm laser frequency, while higher-frequency components for the yield oscillations are found for the electrons emitted perpendicular to the laser polarization direction. By decomposing the photoelectron angular distribution into different partial waves, we found that those near-threshold photoelectrons are generated by the interference of different photon channels via resonant states. Moreover, we observed a large time delay between the near-threshold photoelectrons emitted along the laser polarization direction via the $5p$ and $4f$ resonant states.

DOI: 10.1103/PhysRevA.106.033112

I. INTRODUCTION

When an atom or a molecule is exposed to a strong laser pulse, an electron can be released from the bound state [1–3]. The released electron carries ultrafast dynamical information during photoionization, such as attosecond time delays in photoemission. Various attosecond methodologies have been proposed to extract the dynamical information of photoionization on the attosecond timescale, such as attosecond streaking [4], attoclocks [5,6], photoelectron holography [7–9], and reconstruction of attosecond harmonic beating by interference of two-photon transitions (RABBITT) techniques [10–21]. In the RABBITT technique, an extreme ultraviolet pulse train consisting of odd harmonics of a fundamental infrared (IR) laser is used to ionize a target, leading to single-photon peaks in the photoelectron energy spectrum (main bands). Then a weak IR field triggers continuum-continuum transitions with absorption or emission of an IR photon, generating sidebands between two adjacent main bands [20]. Two different quantum pathways will contribute to the same sideband and thus interfere. The intensity of each sideband oscillates with twice the IR frequency [12,15]; from the phase of the oscillation one can extract the temporal properties of the photoemission process [10].

The RABBITT technique has been used to obtain Wigner time delay in atoms and molecules [19], to measure relative time delays for electron emissions from different atomic levels [12], to demonstrate the influence of spin-orbit coupling on attosecond photoionization delays [17], and to reveal the dependence of the delay of the continuum-continuum transition on the angular momentum of the electron final state [20]. Moreover, the RABBITT technique has also been used to study resonant ionization, in which the phase shift due to an intermediate resonance was mapped out [11]. By studying an angle-resolved near-threshold sideband due to an intermediate resonance, the phases and amplitudes of all partial-wave components that contribute to the continuum wave function are reconstructed using the RABBITT technique [22].

Recently, the RABBITT-type interferometry was extended to the strong-field multiphoton regime [23–30]. In the multiphoton RABBITT experiment, a strong driving laser field with 2ω frequency was used to produce the bound-continuum transition to the above-threshold ionization (ATI) peaks by multiphoton absorption. A weak IR laser field with ω frequency triggers the continuum-continuum transition by absorption or emission of an IR photon from adjacent ATI peaks and opens up interfering pathways to the sidebands [23]. By changing the relative phase between the two-color laser pulses, the intensity of both ATIs and sidebands oscillates with twice the IR frequency. By studying the oscillations of different ATIs and sidebands, the energy-resolved time delay was probed in the ATI regime [23,30]. It was found that the time delay is strongly influenced by the intensities of both ω and 2ω laser pulses [23,30]. Extending the RABBITT interferometry to chiral molecules, an attosecond time delay between electrons ejected forward and backward relative to the laser propagation direction was revealed [31]. The multiphoton RABBITT protocol has also been studied in corotating and counterrotating circularly polarized two-color laser fields from the perspective of the photon-absorption channels [29,32]. Moreover, because resonant excitation or ionization is a general process in the multiphoton regime, the temporal dynamics of the intermediate resonant states has also been probed in the multiphoton regime [24,33,34].

*mli@hust.edu.cn

It was claimed that a time delay for photoemission between two Freeman resonant states in the multiphoton ionization regime was observed using orthogonally polarized two-color laser fields with comparable intensities [24]. However, when the intensities of the ω and 2ω components are comparable, the electron in the continuum state can absorb or emit more than one ω photon, leading to complex photon interfering pathways in forming the sidebands and ATIs. This provides obstacles for a straightforward extraction of attosecond time delays of the photoemission [30]. Furthermore, the near-threshold photoelectron generated via a resonant state in the conventional RABBITT experiment reveals fruitful information about the resonant state, and it can be used for coherent imaging of an attosecond electron wave packet [11,22,35]. However, the ionization dynamics for the near-threshold photoelectron generated via a resonant state has not yet been studied in the multiphoton RABBITT experiment.

In this paper, using the multiphoton RABBITT technique, we study the near-threshold photoelectron of an Ar atom ionized by parallel polarized two-color laser fields consisting of a weak 800-nm field and a strong 400-nm laser field. It is found that the angular distribution of the near-threshold photoelectron from the resonant ionization can be controlled by changing the weak 800-nm laser intensity and the relative phase of the two-color components. By decomposing the photoelectron angular distribution into different partial waves, we show that the near-threshold photoelectrons are produced from resonance-enhanced multiphoton ionization via multiple interference pathways from the ATIs or the resonant bound state. Due to the multipathway interference, the yield of the near-threshold photoelectron oscillates with twice the 800-nm laser frequency in the laser polarization direction, while the yield oscillation contains quadruple the 800-nm frequency component in the direction perpendicular to the laser polarization. We also find that there is a large emission time delay for the near-threshold photoelectrons emitted along the laser polarization direction from the resonance-enhanced ionization via the $5p$ and $4f$ states.

Unless specified otherwise, atomic units are used throughout this paper.

II. EXPERIMENTAL METHODS

Experimentally, the fundamental 800-nm field, generated from a Ti:sapphire femtosecond laser system with a repetition of 5 kHz, is frequency doubled using a 250-μm-thick β-barium borate (β-BBO) crystal to produce 400-nm laser fields. Parallel polarized two-color (PTC) laser fields are produced using a dual-color wave plate, by which the polarization direction of the 800-nm field can be rotated while keeping the polarization direction of the 400-nm field unchanged. The relative phase ϕ between the two-color laser pulses is finely controlled using a pair of fused silica wedges, one of which was mounted on a motorized stage. Then the PTC laser fields are focused onto a supersonic gas jet of Ar in an ultrahigh-vacuum chamber of a cold-target recoil-ion momentum spectroscopy [36] setup by a parabolic mirror ($f = 75$ mm). The generated electrons and ions are accelerated and guided to the microchannel plate detectors along the time-of-flight axis by a weak homogeneous static electric field ($\sim$10.2 V/cm) and magnetic field ($\sim$9.3 G). By measuring the times of flight and the positions of the particles on the detectors, three-dimensional photoelectron and photoion momentum distributions with high resolution can be obtained. For the 400-nm laser intensity, we change the laser intensity to another value corresponding to nonresonant ionization. The laser intensity is calibrated from the energy shift of the nonresonant ATI peak, which is proportional to the ponderomotive potential U_p. For the weak 800-nm laser field, we estimate its intensity from the power ratio between the 400- and 800-nm laser fields, which is measured by a spectrometer. In the experiment, the intensity for the 400-nm laser field is estimated to be $\sim 7.9 \times 10^{13}$ W/cm^2. For the 800-nm laser field, the intensity is adjusted to be $\sim 2.2 \times 10^{12}$ or $\sim 3.2 \times 10^{12}$ W/cm^2 for two different cases.

III. RESULTS AND DISCUSSION

The photoelectron momentum distribution (PEMD) of argon in a single-color 400-nm laser field is shown in Fig. 1(a). In Fig. 1(a), a double-ring structure appears for the first-order ATI. Those two rings correspond to two peaks at 1.8 and 2.2 eV in the photoelectron energy spectrum, which are exactly the same as those in Ref. [24]. Those two peaks come from resonant ionization via the $5p$ and $4f$ states of argon atoms, respectively [24,37]. By adding a relatively weak 800-nm laser field to the strong 400-nm field, the PEMDs are changed, as shown in Figs. 1(c) and 1(d). Figure 1(c) corresponds to an IR intensity of $I_{800} \sim 2.2 \times 10^{12}$ W/cm^2, and Fig. 1(d) corresponds to an IR intensity of $I_{800} \sim 3.2 \times 10^{12}$ W/cm^2. The PEMDs in Figs. 1(c) and 1(d) are integrated over the relative phases varying from zero to 2π. In both cases, there are many near-threshold photoelectrons ($E_k < 1$ eV) in the PEMDs, which do not appear for a single 400-nm field. Here, E_k is the electron energy. Although the 800-nm laser field is weak, the yield of those near-threshold photoelectrons is high. In Fig. 1(b), we show the measured photoelectron energy spectra of Fig. 1(c) (blue dashed lines) and Fig. 1(d) (red solid lines). Those near-threshold photoelectrons reveal two peaks in the photoelectron energy spectra, indicated as peak A and peak B in Fig. 1(b). Peak A appears at $\sim$0.3 eV, and peak B appears at $\sim$0.6 eV. When we change the 800-nm intensity, the positions of those two peaks do not shift. This demonstrates that those two peaks originate from the resonant ionization [34]. Because the energy difference between peak A (peak B) and the $5p$ ($4f$) bound state corresponds to one IR photon energy, peak A (peak B) also comes from the resonant ionization via the $5p$ ($4f$) intermediate state. In Figs. 1(e) and 1(f), we show the near-threshold photoelectron angular distribution in Figs. 1(c) and 1(d). The blue solid lines are the angular distributions of the photoelectron from the $5p$ resonant ionization, and the red dotted lines are the angular distributions of the photoelectrons from the $4f$ resonant ionization. It is found that the angular distribution of the near-threshold photoelectrons via the $5p$ intermediate state varies from a four-lobe structure to an eight-lobe structure with increasing the 800-nm laser intensity, as indicated by the arrows, while the angular distribution of the near-threshold photoelectrons via the $4f$ state reveals an eight-lobe structure for two 800-nm laser intensities.

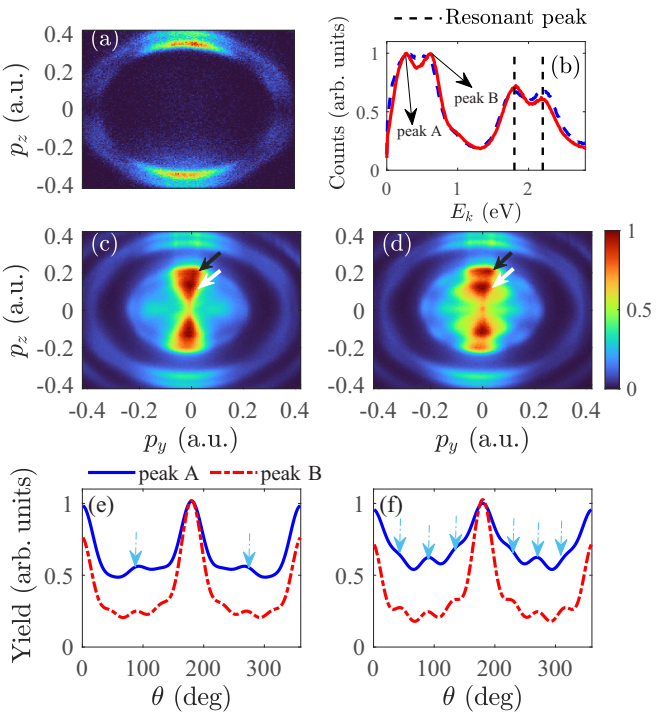

FIG. 1. (a) The PEMD in a single-color 400-nm laser field. The PEMDs in the PTC laser fields with 800-nm laser intensities of (c) 2.2×10^{12} W/cm^2 and (d) 3.2×10^{12} W/cm^2. (b) The measured photoelectron energy spectra of (c) (blue dashed line) and (d) (red solid line). The double-peak structure of the first-order ATI is guided by the two vertical dashed lines. For the near-threshold photoelectrons, there are also two peaks, which are labeled peak A and peak B. Peak A and peak B correspond to the two rings in the PEMDs in (c) and (d), indicated by white arrows and black arrows, respectively. Peak A and Peak B originate from the $5p$ and $4f$ resonant states, respectively. The near-threshold photoelectron angular distribution of the $5p$ resonant ionization in (c) and (d) is shown by the blue solid lines in (e) and (f). The near-threshold photoelectron angular distribution of the $4f$ resonant ionization in (c) and (d) is shown by the red dotted lines in (e) and (f). The arrows in (e) and (f) show the lobe of the angular distribution of the near-threshold photoelectron from the $5p$ resonant ionization. The laser field is polarized along the z-axis direction.

In order to explain the results in Fig. 1, we show in Fig. 2 the energy-level diagram that may be able to rationalize the experimental results. When the atom absorbs several 400-nm photons from the ground state, it will populate into the $5p$ or $4f$ resonant states because of the ac Stark shift. Then the electron in the resonant state can absorb an additional 400-nm photon to form a first-order ATI. In the presence of the weak 800-nm field, the electron can be released either from the resonant states directly by absorbing an IR photon or from the first-order ATI by emitting an IR photon to the sideband. These two channels are labeled pathway I and pathway II in Fig. 2, which will interfere. The interference is very similar to recent studies using a technique called the under-threshold RABBITT protocol in the two-photon process [35].

In order to show clearly how the interference of the near-threshold photoelectron manifests itself in the photoelectron angular distribution, we illustrate the PEMDs at different

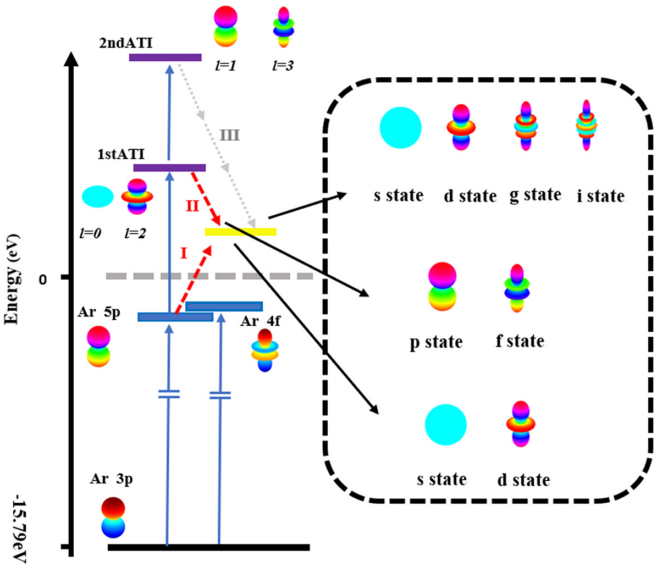

FIG. 2. The energy diagram shows the levels that are relevant for understanding the origin of the near-threshold photoelectrons. The thick blue lines show the $5p$ and $4f$ resonant states, and the purple lines show the first-order ATI and second-order ATI. The thick yellow line shows the sideband corresponding to the near-threshold photoelectron. Different 800-nm photon transition pathways from the $5p$ bound state, the first-order ATI, and the second-order ATI are represented by the red dashed arrows (labeled I and II) and the gray dotted arrows (labeled III), leading to different partial waves for the near-threshold photoelectrons for different interference pathways.

relative phases in Fig. 3. Depending on the relative phase, the PEMDs reveal clear up-down asymmetries in the two-color laser field. We also show in Fig. 4(a) the measured near-threshold photoelectron angular distribution of the $5p$ resonant ionization as a function of the relative phase between the two-color components with an 800-nm laser intensity of $\sim 2.2 \times 10^{12}$ W/cm^2. It is clear that the yield oscillates with

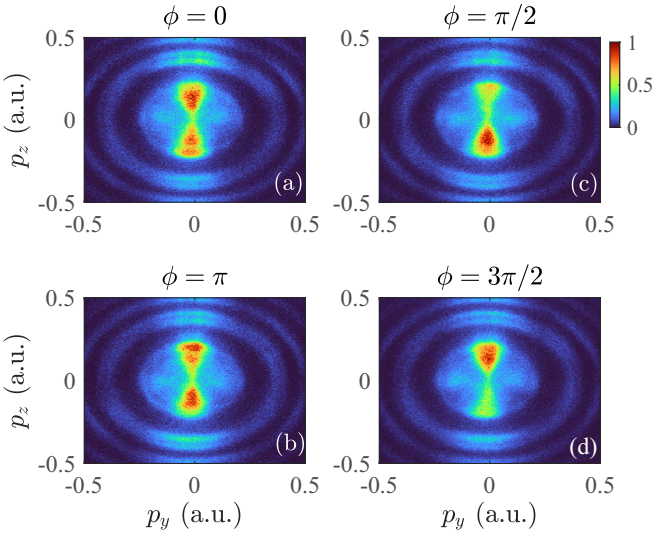

FIG. 3. The PEMDs in the PTC laser fields with an 800-nm laser intensity of 2.2×10^{12} W/cm^2 at different relative phases of (a) $\phi = 0$, (b) $\phi = \pi/2$, (c) $\phi = \pi$, and (d) $\phi = 3\pi/2$.

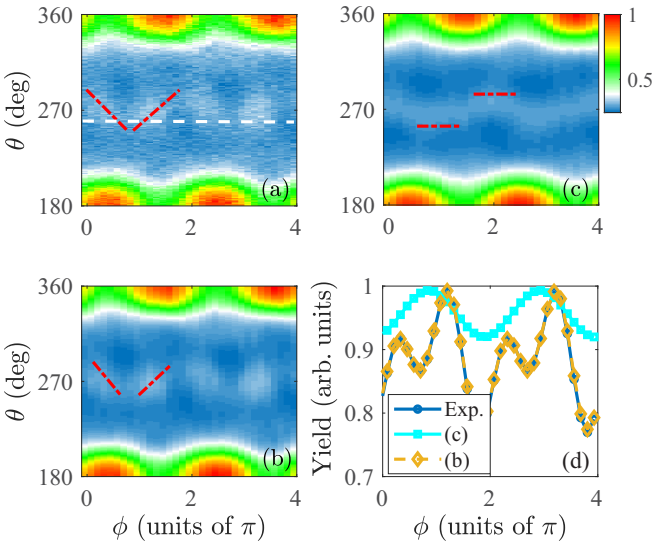

FIG. 4. (a) The measured phase-resolved photoelectron angular distribution for the near-threshold photoelectrons via the $5p$ intermediate state. The intensity for the 800-nm laser field is $I_{800} \sim 2.2 \times 10^{12}$ W/cm^2. (b) The reconstructed phase-resolved photoelectron angular distribution using the Legendre polynomial expansion according to Eq. (1). (c) The same as (b), but without considering the interference of pathway I and pathway III in Fig. 2. (d) Comparison of the cut lines taken from (a)–(c) at an emission angle of ∼263°, as indicated by the white dashed line in (a). The red dash-dotted lines in (a)–(c) are used to show the patterns that are nearly perpendicular to the laser polarization direction.

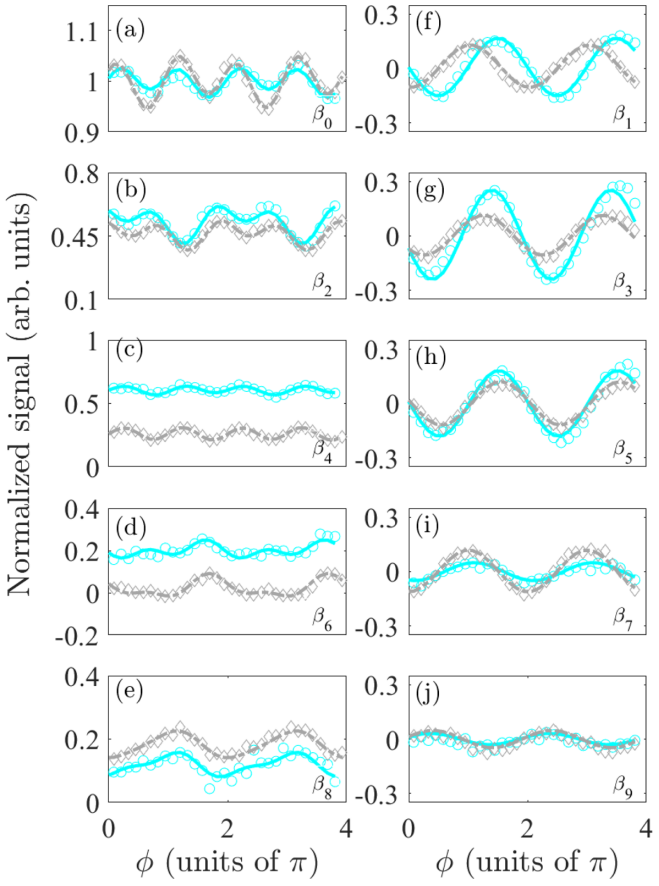

FIG. 5. The coefficients associated with the Legendre polynomials of the $5p$ resonant ionization as a function of the two-color relative phase. The circles show the result of the $5p$ resonant ionization in Fig. 2(c) ($I_{800} \sim 2.2 \times 10^{12}$W/cm^2), while the rhombuses show the result of the $5p$ resonant ionization in Fig. 2(d) ($I_{800} \sim 3.2 \times 10^{12}$ W/cm^2). Those coefficients have been normalized to the average value of β_0. The solid and dashed lines show the fitting results.

twice the 800-nm frequency in the direction parallel to laser polarization in Fig. 4(a). However, for the electron emitted nearly perpendicular to the laser polarization direction, we can see that the yield oscillations contain higher-frequency components. To clearly see this phenomenon, we show in Fig. 4(d) the yield integrated within the emission angle range [258°, 268°] as a function of the relative phase between the two-color components (blue solid line with circles). It is obvious in Fig. 4(d) that the yield oscillation curve contains quadruple the 800-nm frequency component in the direction nearly perpendicular to the laser polarization. Moreover, it is noted that a tilted structure appears near the perpendicular direction, as guided by the red dash-dotted lines in Fig. 4(a).

According to the energy-level diagram in Fig. 2, the interference between pathway I and pathway II will lead to a yield oscillation with twice the 800-nm frequency. In order to explain the origin of higher-frequency components for the yield oscillations perpendicular to the laser polarization direction, we decompose the photoelectron angular distribution into different partial waves. Generally, the total continuum-state wave function is composed of a coherent sum of different partial-waves components, i.e., a sum of spherical harmonics $a_{l,m}Y_l^m$, where the complex amplitude $a_{l,m}$ represents the amplitude and phase of each partial wave. Because the square of the spherical harmonics can be expressed as a sum of Legendre polynomials, the square modulus of the total continuum-state wave function can be expressed as a sum of the Legendre polynomials [13,15,20]. Therefore, the angular distribution of the near-threshold photoelectrons can be expressed as [13,20,22]

$$I(\theta, \tau) = \sum_{n=0}^{2l_{\max}} \beta_n(\phi) P_n[\cos(\theta)], \tag{1}$$

where n is an integer and $l_{\max}$ is the highest angular momentum number of all partial waves. $P_n[\cos(\theta)]$ is the n-order Legendre polynomials, where θ is the angle between the laser polarization and the direction of the outgoing electron. β_n is the expansion coefficients of the n-order Legendre polynomials, which are related to the amplitude and phase of different partial waves. ϕ is the relative phase between the two-color laser pulses. We obtain the parameter β by projecting the measured angular distributions of the near-threshold photoelectrons to the corresponding Legendre polynomials in each relative phase. The parameter β up to ninth-order Legendre polynomials for the $5p$ resonant ionization at different 800-nm intensities is shown in Fig. 5. We have checked that the contributions of all higher-order Legendre polynomials are negligible. In Figs. 5(a)–5(e), we show β for the even-order Legendre polynomial, while β for the odd-order

Legendre polynomial are shown in Figs. 5(f)–5(j). The results are normalized to the averaged value of β_0. It can be found in Fig. 5 that the odd-order β mainly oscillate with twice the 800-nm frequency, while the even-orders β mainly oscillate with quadruple the 800-nm frequency. Because the even-order and odd-order β as a function of the relative phase oscillate with different frequencies, we fit the oscillation of even-order and odd-order parameters with different fitting functions, i.e., $\beta_{n,n=2k} = A_{0,n} + A_{1,n}\cos(2\omega\phi + \Phi_{1,n}) + A_{2,n}\cos(4\omega\phi + \Phi_{2,n})$ and $\beta_{n,n=2k-1} = A_{0,n} + A_{1,n}\cos(2\omega\phi + \Phi_{1,n})$, where k is an integer. Here, $A_{0,n}$ is the averaged value of β_n. $A_{1,n}$ and $\Phi_{1,n}$ are the amplitude and phase shift of twice the 800-nm frequency component. $A_{2,n}$ and $\Phi_{2,n}$ are the amplitude and phase shift of quadruple the 800-nm frequency component.

Assuming that the near-threshold photoelectrons are contributed by only pathway I and pathway II, the odd-order β should oscillate at twice the 800-nm frequency, while the even-order β should be constant because of the opposite parities of the partial waves for pathway I and pathway II [20,23]. As shown in Figs. 5(f)–5(j), due to the orbital parity mix interference, the odd-order β are nonzero in the two-color laser field, leading to the asymmetric PEMDs in Fig. 3 [13,23]. However, the even-order β mainly oscillate with quadruple the 800-nm frequency in Figs. 5(a)–5(e). It is reasonable that the continuum-continuum transition pathway of emission of three 800-nm photons from the second-order ATI makes a significant contribution to the near-threshold photoelectron, as shown by pathway III in Fig. 2 [38,39]. The interference between pathway I and pathway III will generate a yield oscillation signal with quadruple the 800-nm frequency. Moreover, the parities of the partial waves for pathway I and pathway III are both even parities. So the interference of those two pathways will contribute to only the even-order Legendre polynomials. As a result, the even-order β oscillate with quadruple the 800-nm frequency, while the odd-order β does not. Therefore, considering three interference pathways in Fig. 2 is consistent with the observations in Figs. 4 and 5. Moreover, it is noted that the even-order β contain twice the 800-nm frequency component, especially for β_6 and β_8. This might come from the contribution of the nonresonant pathway to the PEMD [40], which is ignored in our study. For the $4f$ resonant ionization, β at different 800-nm intensities are shown in Fig. 6, where the results are also similar to those for the $5p$ resonant ionization. By decomposing the photoelectron angular distribution into a series of Legendre polynomials, we can separate the interference of the even-parity partial waves with the odd-parity partial waves and the interference of the even-parity partial waves with the even-parity partial waves.

The angle-dependent yield oscillations in Fig. 4(a) can be explained by the wave function of the partial waves in different interference pathways, as shown in Fig. 2. On the one hand, the interference between pathway I and pathway II is dominant, and the partial waves reveal a maximum in the direction parallel to the laser polarization. Thus, the yield oscillation with twice the 800-nm frequency is dominant in the direction parallel to the laser polarization. On the other hand, in the direction perpendicular to the laser polarization, the partial waves from pathway II reveal a minimum (odd parity), whereas the partial waves from pathway I and pathway III reveal a maximum (even parity). Therefore, quadruple

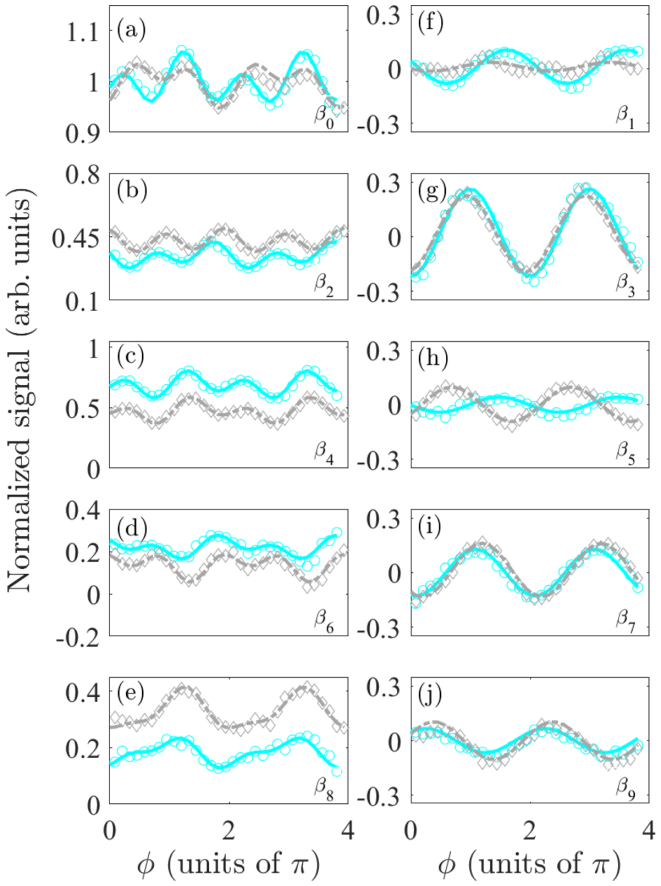

FIG. 6. The same as Fig. 5, but for the $4f$ resonant ionization.

the 800-nm frequency component is comparable to twice the 800-nm frequency component in the direction perpendicular to the laser polarization by considering the interference of all pathways. So the angle-dependent yield oscillation is closely related to the parity of the partial waves in different interference pathways. Because of the importance of quadruple the 800-nm frequency component in the direction perpendicular to the laser polarization, we also show in Fig. 4(c) the reconstructed phase-resolved photoelectron angular distribution without considering the interference between pathway I and pathway III by removing the oscillation of the even-order parameters in Figs. 5(a)–5(e). The reconstructed phase-resolved photoelectron angular distribution is shown in Fig. 4(b) while considering all kinds of interference. The cut lines taken from Figs. 4(b) and 4(c) at the emission angle of 263° are shown in Fig. 4(d). The reconstructed results without considering the interference of pathway I and pathway III are significantly different from the experiment. The tilted structure in Fig. 4(c) disappears in the direction perpendicular to the laser polarization. This indicates that the interference between pathway I and pathway III plays an important role for the tilted structure in the direction nearly perpendicular to the laser polarization.

According to the results in Fig. 5, we can also explain why the angular distribution of the near-threshold photoelectrons via the $5p$ intermediate state varies from a four-lobe structure to an eight-lobe structure with an increase of the 800-nm laser intensity, which is closely related to β_8 in Fig. 5. We can

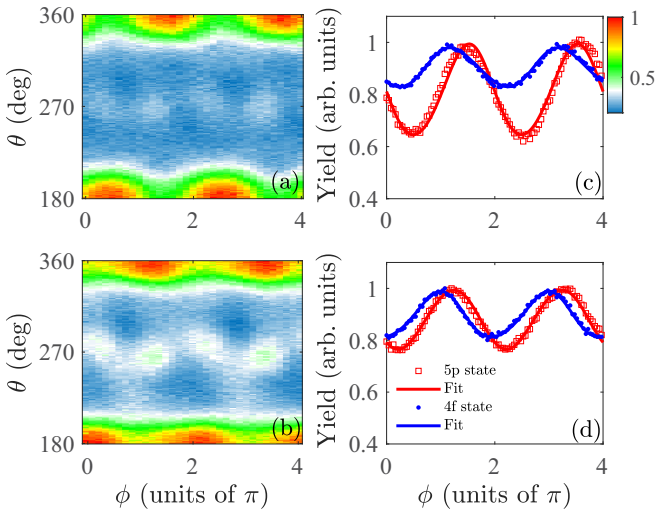

FIG. 7. (a) and (b) The measured phase-resolved photoelectron angular distributions for the $5p$ resonant ionization and the $4f$ resonant ionization for an 800-nm intensity of $I_{800} \sim 2.2 \times 10^{12}$ W/cm^2, respectively. (a) is the same as Fig. 4(a). (c) Comparison of the photoelectron yield oscillations for (a) and (b) within the emission angle range [0°, 30°]. (d) The same as (c), but for an 800-nm intensity of $I_{800} \sim 3.2 \times 10^{12}$ W/cm^2.

see that the value of β_8 increases with increasing the 800-nm intensity, which happens because the relative contribution of pathway III increases with increasing the 800-nm intensity. However, for the $4f$ resonant ionization, the value of β_8 is large for two different 800-nm intensities in Fig. 6, and thus, the angular distribution for the $4f$ resonant ionization is only slightly changed with an increase of the 800-nm intensity.

We further compare the temporal property of the photoelectron emission from different resonant states. In Figs. 7(a) and 7(b), we show a comparison of the measured photoelectron angular distributions of the $5p$ resonant ionization and the $4f$ resonant ionization as a function of the two-color relative phase. An obvious phase shift is observed for the photoelectrons emitted parallel to the laser polarization direction by comparing Figs. 7(a) and 7(b). In order to extract the phase shift, we remove quadruple the 800-nm frequency component from the photoelectron angular distribution in Fig. 4(c). The yields of the photoelectrons emitted along the laser polarization direction as a function of two-color phase delay are shown in Figs. 7(c) and 7(d) for the $5p$ and $4f$ resonant ionizations for two different 800-nm laser intensities. The extracted phase differences between the $5p$ and $4f$ resonant ionizations are about $0.29\pi \pm 0.06\pi$ and $0.26\pi \pm 0.06\pi$ for 800-nm laser intensities of $I_{800} \sim 2.2 \times 10^{12}$ and $I_{800} \sim 3.2 \times 10^{12}$ W/cm^2, respectively. The time delays can be estimated according to the relation $\tau_{ij} = (\delta\phi_{ij})/\omega_{400}$ and are $\sim 190 \pm 40$ and $\sim 170 \pm 40$ as between the $5p$ and $4f$ resonant ionization channels for two different 800-nm intensities, respectively.

We next estimate the phase difference from the theoretical perspective. In the direction parallel to the laser polarization, the interference between pathway I and pathway II is dominant. Thus, we ignore the contribution from pathway III. By neglecting the influence of the transition from the ground state to the resonant state, the ionization time delay is mainly contributed by the Wigner delay and the continuum-continuum transition delay. In our experimental condition, the continuum-continuum transition delay dominates over the Wigner delay for the near-threshold photoelectron. So we need to estimate only the continuum-continuum transition phase of pathway II. The continuum-continuum phase can be calculated based on perturbation theory, $\phi_{cc} = \arg(\frac{(2\kappa)^{iZ/\kappa}}{(2k)^{iZ/k}} \frac{\Gamma[2+iZ(1/\kappa-1/k)]}{(\kappa-k)^{iZ(1/\kappa-1/k)}})$ [15,39,41], where κ is the momentum of the initial state in the continuum, k is the momentum of the final state after the exchange of one fundamental photon, and Z is the remaining charge on the parent ion. Then we can obtain the continuum-continuum transition phase difference for the photoelectron from the $5p$ resonant ionization and the $4f$ resonant ionization. We estimate that the continuum-continuum transition phase difference for the photoelectron from the $5p$ resonant ionization and the $4f$ resonant ionization is $\sim 0.25\pi$ under our experimental condition. It is nearly consistent with our measured results. So the large time delay extracted from the experiment might originate mainly from the continuum-continuum transition, rather than the dwell time in the resonant state [24,25]. In Fig. 2, all pathways go through the resonant states. As a result, the time delay in the resonant states will not manifest in the interference signals of those pathways.

IV. CONCLUSIONS

In conclusion, we have studied the near-threshold photoelectrons of argon atoms emitted from the $5p$ and $4f$ intermediate states in the multiphoton RABBITT experiment in PTC laser fields consisting of a strong 400-nm laser field and a weak 800-nm laser field. We showed that those near-threshold photoelectrons are produced from multipathway interference via resonance-enhanced ionization. By decomposing the photoelectron angular distribution into a series of the Legendre polynomials, we can separate the interference of partial waves with even-odd parities and the interference of partial waves with even-even parities. We found that the odd-order β of the Legendre polynomials oscillate with twice the 800-nm frequency, while the even-order β mainly oscillate with quadruple the 800-nm frequency. We further find that there is a large time delay between the photoelectrons via the $5p$ and $4f$ resonant state ionizations for an electron emitted along the laser polarization direction. This study has implications for studying a near-threshold photoelectron originating from multipathway interference via resonance-enhanced ionization. It will facilitate studies about coherent imaging of the photoelectron continuum state wave function in the multiphoton regime [22].

ACKNOWLEDGMENTS

This work was supported by the National Key Research and Development Program of China (Grant No. 2019YFA0308300) and the National Natural Science Foundation of China (Grant No. 12021004). The computation was completed in the HPC Platform of Huazhong University of Science and Technology.

[1] P. B. Corkum, Plasma Perspective on Strong Field Multiphoton Ionization, Phys. Rev. Lett. **71**, 1994 (1993).

[2] M. Protopapas, C. H. Keitel, and P. L. Knight, Atomic physics with super-high intensity lasers, Rep. Prog. Phys. **60**, 389 (1997).

[3] F. Krausz and M. Ivanov, Attosecond physics, Rev. Mod. Phys. **81**, 163 (2009).

[4] J. Itatani, F. Quéré, G. L. Yudin, M. Y. Ivanov, F. Krausz, and P. B. Corkum, Attosecond Streak Camera, Phys. Rev. Lett. **88**, 173903 (2002).

[5] P. Eckle, A. N. Pfeiffer, C. Cirelli, A. Staudte, R. Dörner, H. G. Muller, M. Büttiker, and U. Keller, Attosecond ionization and tunneling delay time measurements in helium, Science **322**, 1525 (2008).

[6] L. Torlina, F. Morales, J. Kaushal, I. Ivanov, A. Kheifets, A. Zielinski, A. Scrinzi, H. G. Muller, S. Sukiasyan, M. Ivanov, and O. Smirnova, Interpreting attoclock measurements of tunnelling times, Nat. Phys. **11**, 503 (2015).

[7] Y. Huismans *et al.*, Time-resolved holography with photoelectrons, Science **331**, 61 (2011).

[8] Y. Zhou, O. I. Tolstikhin, and T. Morishita, Near-Forward Rescattering Photoelectron Holography in Strong-Field Ionization: Extraction of the Phase of the Scattering Amplitude, Phys. Rev. Lett. **116**, 173001 (2016).

[9] M. Li, H. Xie, W. Cao, S. Luo, J. Tan, Y. Feng, B. Du, W. Zhang, Y. Li, Q. Zhang, P. Lan, Y. Zhou, and P. Lu, Photoelectron Holographic Interferometry to Probe the Longitudinal Momentum Offset at the Tunnel Exit, Phys. Rev. Lett. **122**, 183202 (2019).

[10] P. M. Paul, E. S. Toma, P. Breger, G. Mullot, F. Augé, P. Balcou, H. G. Muller, and P. Agostini, Observation of a train of attosecond pulses from high harmonic generation, Science **292**, 1689 (2001).

[11] M. Swoboda, T. Fordell, K. Klünder, J. M. Dahlström, M. Miranda, C. Buth, K. J. Schafer, J. Mauritsson, A. L'Huillier, and M. Gisselbrecht, Phase Measurement of Resonant Two-Photon Ionization in Helium, Phys. Rev. Lett. **104**, 103003 (2010).

[12] K. Klünder, J. M. Dahlström, M. Gisselbrecht, T. Fordell, M. Swoboda, D. Guénot, P. Johnsson, J. Caillat, J. Mauritsson, A. Maquet, R. Taïeb, and A. L'Huillier, Probing Single-Photon Ionization on the Attosecond Time Scale, Phys. Rev. Lett. **106**, 143002 (2011).

[13] G. Laurent, W. Cao, H. Li, Z. Wang, I. Ben-Itzhak, and C. L. Cocke, Attosecond Control of Orbital Parity Mix Interferences and the Relative Phase of Even and Odd Harmonics in an Attosecond Pulse Train, Phys. Rev. Lett. **109**, 083001 (2012).

[14] K. L. Ishikawa and K. Ueda, Competition of Resonant and Nonresonant Paths in Resonance-Enhanced Two-Photon Single Ionization of He by an Ultrashort Extreme-Ultraviolet Pulse, Phys. Rev. Lett. **108**, 033003 (2012).

[15] J. M. Dahlström, D. Guénot, K. Klünder, M. Gisselbrecht, J. Mauritsson, A. L'Huillier, A. Maquet, and R. Taïeb, Theory of Attosecond Delays in Laser-Assisted Photoionization, Chem. Phys. **414**, 53 (2013).

[16] S. Heuser, Á. Jiménez Galán, C. Cirelli, C. Marante, M. Sabbar, R. Boge, M. Lucchini, L. Gallmann, I. Ivanov, A. S. Kheifets, J. M. Dahlström, E. Lindroth, L. Argenti, F. Martïn, and U. Keller, Angular dependence of photoemission time delay in helium, Phys. Rev. A **94**, 063409 (2016).

[17] I. Jordan, M. Huppert, S. Pabst, A. S. Kheifets, D. Baykusheva, and H. J. Wörner, Spin-orbit delays in photoemission, Phys. Rev. A **95**, 013404 (2017).

[18] L. Cattaneo, J. Vos, R. Y. Bello, A. Palacios, S. Heuser, L. Pedrelli, M. Lucchini, C. Cirelli, F. Martín, and U. Keller, Attosecond coupled electron and nuclear dynamics in dissociative ionization of H_2, Nat. Phys. **14**, 733 (2018).

[19] J. Vos, L. Cattaneo, S. Patchkovskii, T. Zimmermann, C. Cirelli, M. Lucchini, A. Kheifets, A. S. Landsman, and U. Keller, Orientation-dependent stereo Wigner time delay and electron localization in a small molecule, Science **360**, 1326 (2018).

[20] J. Fuchs, N. Douguet, S. Donsa, F. Martin, J. Burgdörfer, L. Argenti, L. Cattaneo, and U. Keller, Time delays from one-photon transitions in the continuum, Optica **7**, 154 (2020).

[21] J.-B. Ji, S. Heck, M. Han, and H. J. Wörner, Quantitative uncertainty determination of phase retrieval in RABBITT, Opt. Express **29**, 27732 (2021).

[22] D. M. Villeneuve, P. Hockett, M. J. J. Vrakking, and H. Niikura, Coherent imaging of an attosecond electron wave packet, Science **356**, 1150 (2017).

[23] L. J. Zipp, A. Natan, and P. H. Bucksbaum, Probing electron delays in above-threshold ionization, Optica **1**, 361 (2014).

[24] X. Gong, C. Lin, F. He, Q. Song, K. Lin, Q. Ji, W. Zhang, J. Ma, P. Lu, Y. Liu, H. Zeng, W. Yang, and J. Wu, Energy-Resolved Ultrashort Delays of Photoelectron Emission Clocked by Orthogonal Two-Color Laser Fields, Phys. Rev. Lett. **118**, 143203 (2017).

[25] P. Ge, M. Han, M.-M. Liu, Q. Gong, and Y. Liu, Probing time delays and coherent imaging of multiphoton resonant ionization, Phys. Rev. A **98**, 013409 (2018).

[26] Y. Feng, M. Li, S. Luo, K. Liu, B. Du, Y. Zhou, and P. Lu, Semiclassical analysis of photoelectron interference in a synthesized two-color laser pulse, Phys. Rev. A **100**, 063411 (2019).

[27] M. Han, H. Liang, P. Ge, Y. Fang, Z. Guo, X. Yu, Y. Deng, L. Y. Peng, Q. Gong, and Y. Liu, Timing angular momentum transfer for parity-unfavored transitions in multiphoton ionization, Phys. Rev. A **102**, 061101(R) (2020).

[28] D. You *et al.*, New Method for Measuring Angle-Resolved Phases in Photoemission, Phys. Rev. X **10**, 031070 (2020).

[29] P. Ge, Y. Fang, Z. Guo, X. Ma, X. Yu, M. Han, C. Wu, Q. Gong, and Y. Liu, Probing the Spin-Orbit Time Delay of Multiphoton Ionization of Kr by Bicircular Fields, Phys. Rev. Lett. **126**, 223001 (2021).

[30] S. D. López, S. Donsa, S. Nagele, D. G. Arbó, and J. Burgdörfer, Phase delays in $\omega - 2\omega$ above-threshold ionization, Phys. Rev. A **104**, 043113 (2021).

[31] S. Beaulieu, A. Comby, A. Clergerie, J. Caillat, D. Descamps, N. Dudovich, B. Fabre, R. Géneaux, F. Légaré, S. Petit, B. Pons, G. Porat, T. Ruchon, R. Taïeb, V. Blanchet, and Y. Mairesse, Attosecond-resolved photoionization of chiral molecules, Science **358**, 1288 (2017).

[32] Q.-H. Ke, Y.-M. Zhou, Y.-J. Liao, J.-T. Liang, Y. Zhao, J. Tan, M. Li, and P.-X. Lu, Helicity-dependent time delays in multiphoton ionization by two-color circularly polarized laser fields, Front. Phys. **16**, 52503 (2021).

[33] X. Song, G. Shi, G. Zhang, J. Xu, C. Lin, J. Chen, and W. Yang, Attosecond Time Delay of Retrapped Resonant Ionization, Phys. Rev. Lett. **121**, 103201 (2018).

[34] R. R. Freeman, P. H. Bucksbaum, H. Milchberg, S. Darack, D. Schumacher, and M. E. Geusic, Above-Threshold Ionization with Subpicosecond Laser Pulses, Phys. Rev. Lett. **59**, 1092 (1987).

[35] A. S. Kheifets and A. W. Bray, RABBITT phase transition across the ionization threshold, Phys. Rev. A **103**, L011101 (2021).

[36] J. Ullrich, R. Moshammer, A. Dorn, R. Dörner, L. P. H. Schmidt, and H. Schmidt-Böcking, Recoil-ion and electron momentum spectroscopy: Reaction-microscopes, Rep. Prog. Phys. **66**, 1463 (2003).

[37] R. Wiehle, B. Witzel, H. Helm, and E. Cormier, Dynamics of strong-field above-threshold ionization of argon: Comparison between experiment and theory, Phys. Rev. A **67**, 063405 (2003).

[38] P. K. Maroju *et al.*, Attosecond pulse shaping using a seeded free-electron laser, Nature (London) **578**, 386 (2020).

[39] D. Bharti, D. Atri-Schuller, G. Menning, K. R. Hamilton, R. Moshammer, T. Pfeifer, N. Douguet, K. Bartschat, and A. Harth, Decomposition of the transition phase in multi-sideband schemes for reconstruction of attosecond beating by interference of two-photon transitions, Phys. Rev. A **103**, 022834 (2021).

[40] P. Stammer, S. Patchkovskii, and F. Morales, Evidence of ac-Stark-shifted resonances in intense two-color circularly polarized laser fields, Phys. Rev. A **101**, 033405 (2020).

[41] X. Yu, M. Han, Z. Guo, and Y. Liu, Intrinsic resonant photoionization time delay of hydrogen atoms probed with attosecond beating of asymmetrical photon transitions, Phys. Rev. A **104**, 063108 (2021).